Outstanding dispersion of CeO_2 on Reduced Graphene Oxide. Implications for Highly Dispersed Pd Catalysts

Carlos A. Franchini, Jordi Llorca[a], Alexei Kuznetsov[b] and Adriana M. Silva[c,*]

[a]Institute of Energy Technologies, Department of Chemical Engineering and Barcelona Research Center in Multiscale Science and Engineering, Universitat Politècnica de Catalunya, EEBE, Eduard Maristany 10-14, 08019 Barcelona, Spain

[b]Divisão de Metrologia de Materiais, Instituto Nacional de Metrologia, Qualidade e Tecnologia (INMETRO), Duque de Caxias, RJ, 25250-020, Brazil

[c]Laboratório Associado de Combustão e Propulsão, Instituto Nacional de Pesquisas Espaciais (INPE), Cachoeira Paulista, SP, 12630-000, Brazil.

[*]Corresponding author: adriana.silva@inpe.br

Abstract

In this contribution, we report a totally new and an unprecedented capability of producing nano-CeO_2 evenly dispersed over reduced graphene oxide (rGO), enabling an extremely high dispersion of Pd at high loading (~ 5 %wt) in the catalyst, in one-step hydrothermal synthesis. Morphology and thermal stability of the synthesized Pd/CeO_2-rGO system are compared with Pd/rGO counterpart. High-resolution transmission microscopy studies of synthesized samples combined with X-ray diffraction, Raman and thermal analyses showed the formation of sub-nanometer Pd clusters on nano-CeO_2 dispersed over reduced graphene oxide (rGO). Notably, rGO had a decisive role over the stabilization of CeO_2 as nano-structures, leading to the outstanding Pd dispersion on this catalyst.

Keywords: Pd sub-nanometer dispersion; reduced graphene oxide (rGO); nanosized CeO_2; rGO-CeO_2 and Pd-CeO_2 interactions

1. Introduction

Catalysts, composed of supported metal or metal oxide particles with respective sizes restricted to few nanometers (< 10 nm) and narrow particle-size distribution (nanoclusters) are crucial for optimal catalytic performance [1, 2]. The low-coordinated atoms in such nanoclusters act as active sites for specific catalytic reactions [1]. High dispersion of an active metal phase on an appropriate support increases its specific surface area and, therefore, the interface for adsorption of reactants with subsequent reactions. Mainly, high dispersion of metal particles defines the high catalytic activity of such a system. Although, classical preparation protocols of catalysts are well-investigated and optimized [3], the poor control over the metallic dispersion and metal sintering motivated a considerable number of studies on size reduction and stability/durability of metal clusters in different catalysts systems (see Liu [4, 5] and references therein). However, the attainment of a high dispersion of metallic particles (nanoclustering) on high-surface-area supports is extremely difficult and in practice, the supported metal nanoclusters are heterogeneously distributed on the accessible surface of the support with a considerable variation in their sizes and atomic configuration [4, 5].

Different strategies have been developed for downsizing the metal particles of supported catalyst up to the single atom scale defining thus several types of highly dispersed metallic, such as catalysts as single-atom catalysts, atomically dispersed supported metal catalysts, single site heterogeneous catalysts and site-isolated heterogeneous catalysts [4, 5]. Despite the considerable achievements in synthesis methods for producing catalysts with the novel atom-scale design, the development of a non-expensive and highly dispersed catalyst with high metal loading is still an ongoing task [5]. The effective approach to developing such practical highly dispersed catalysts

should invariably rely on an engineering of anchoring sites on the support surfaces and a strong interaction between the metal atoms and anchoring sites [4].

Carbonaceous materials, especially graphene-based materials such as reduced graphene oxide (rGO), are promising and extensively studied supports for highly dispersed metallic catalysts [6]. The ultimate surface area limit (2600 m^2/g) and the presence of vacancies, remaining oxygen, sulfur and/or nitrogen atoms, which serve as anchoring sites for metal atoms, are the main attractive features of graphene-based supports [6]. All these characteristics have motivated the development of different rGO-metal hybrids with the purpose of controlling the sizes and shape of the metallic particles [7]. Nonetheless, the high metallic dispersion on graphene or other carbon-rich supports suffers from few fundamental issues, characteristic also for metal oxides supports, namely, cumbersome synthesis (imposing subsequent scalability and cost issues in practical applications) and/or limited loads (<0.2 wt%) of stabilized metal atoms or clusters [8].

In this contribution, we report a one-step synthesis of highly dispersed Pd on CeO_2-rGO support using a conventional hydrothermal method. The positive role of ceria over the metallic dispersion [9] and prevention from sintering, as well as a stabilization of noble metals on CeO_2 in a single atom configuration is well documented [10]. The stability of single metal atoms and subnanoclusters on CeO_2 depends on the morphology and dimension of the ceria surface [10]. Size-induced effects like oxygen transfer between metal-ceria interface [11] and lattice relaxation of CeO_2 crystal, associated to a reduction of the valence of Ce [12], promote a stabilization of small clusters of active phases on small domains of ceria supports. Consequently, the main premise of this study was a production of a CeO_2-rGO composite with highly dispersed nanosized CeO_2 domains that, in turn, stabilize smaller Pd species. The choice of

hydrothermal method for the synthesis was governed by several factors. Firstly, a number of successful syntheses of CeO_2-rGO nanocomposites by hydrothermal technique have been reported [13-15]. Secondly, the hydrothermal synthesis is a simple and a feasible method of the catalysts production at the large scale [16]. The reported results show that the employed hydrothermal processing indeed produces a novel nearly continuous coating of rGO flakes by nanostructured CeO_2 domains with a simultaneous fixation of the atomically structured Pd on such a support.

2. Experimental

2.1. Catalysts Preparation

GO precursors

Graphene oxide (GO) was prepared following a modified Hummers method [17]. Briefly, 3 g of graphite powder (Sigma-Aldrich) were poured to 70 mL of concentrated H_2SO_4 (Merck) under stirring at the room temperature. Afterwards, the 1.5 g of $NaNO_3$ (Vetec) were added to the mixture kept in an ice bath to avoid the temperature rise. The 9 g of $KMnO_4$ (Vetec) were slowly added to keep the reaction temperature below 20 °C. The produced mixture was warmed up to 35 °C and maintained at this temperature in a water bath for 30 min resulting in a thick paste. Then, 140 mL of water was poured into the paste and the resulting mixture was kept under stirring for 15 min. Subsequently, additional 500 mL of water was added, followed by the addition of 20 mL of H_2O_2 (30%) (Vetec). At this step, the color of produced slurry changed from brown to yellow. The obtained product was filtered and washed with 250 mL of 10% HCl (Sigma-Aldrich) aqueous solution with the aim of removing metallic ions. After that, the final slurry was repeatedly washed and centrifuged to remove supernatant impurities, until the pH of supernatant water reached 5.5.

rGO support and rGO catalysts

The reduced graphene oxide (rGO) synthesis was carried out by taking 34.4 mL of an aqueous solution of GO (2.03 g/mL) and sonicating it in ultrasonic bath for 2 hours [17]. Then, the GO water dispersion was put in a teflon-lined autoclave, sealed and maintained at 180 °C, for 16 hours. The obtained rGO was a black-colored compacted cylinder immiscible in a water residue. The solid cylinder was removed from the water with tweezers and dried under room temperature for two days.

Analogously, the hydrothermal synthesis of the catalysts were performed using an aqueous solution of GO (2.03 g/mL) and $Pd(NO_3)_2*2H_2O$ in proportion required for preparation of 5 wt% loading of Pd in both catalysts, Pd/rGO and Pd/Ce-rGO. For the synthesis of the catalyst Pd/CeO_2-rGO, it was also added $Ce(NO_3)_2*6H_2O$ aiming at reaching of 30 wt% loading of Ce. The conditions of the hydrothermal synthesis were the same as described for the rGO preparation. In order to isolate the effect of CeO_2 in Pd/CeO_2-rGO system on respective thermal properties, the Ce-rGO sample was also prepared following the same procedure of hydrothermal synthesis of Pd/Ce-rGO catalyst, with no $Pd(NO_3)_2*2H_2O$ in the initial aqueous solution of GO.

2.2. Catalysts Characterization

N_2 Physisorption

The N_2 adsorption measurements were carried out at -196°C on NOVA 2200e surface area analyser, from Quantachrome Instruments. After adsorption–desorption experiments, the catalysts were outgassed at 200°C for 2 hours. Specific surface areas of the studied samples were calculated from adsorption isotherms by applying the BET formalism to the acquired data.

X-ray Diffraction (XRD)

XRD patterns were recorded on a D8 Focus diffractometer from Bruker using Cu-Kα radiation (Ni filter, $\lambda_{K\alpha 1}$ = 1.5406 Å). The diffraction patterns were obtained at the room temperature over 2θ range from 10° to 100° with 2θ step of 0.02. The diffractometer was equipped with an Anton Paar TTK-450 chamber with temperature and atmosphere control. All powder diffraction patterns were collected at 25 °C, under a He flow of 20 mL/min.

Transmission Electron Microscopy – TEM

The transmission electron microscopy analyses were done using a high-resolution electron microscopy FEI Tecnai F20, equipped with a field emission electron gun, operating at 200 kV. The samples for TEM were prepared by dispersing the powder catalysts in an alcohol suspension. Then, a drop of the dispersion was placed over a grid with lacey-carbon film.

Thermogravimetric Analysis/Mass Spectrometry

Thermal analysis were carried out in a TA analyzer (STA 443 Jupiter/Netzsch) by heating the sample from the room temperature to 800 °C (heating rate of 5 °C/min) under air flow. The exiting gas from TGA was analyzed by a Mass Spectrometer (QMS 403 D Aeolos/Netzsch). The monitored mass-to-charge ratios, m/z, were 18, 28 and 44, related to losses of H_2O, CO and CO_2, respectively.

Raman Spectroscopy

Raman spectra were recorded from different regions of each sample at room temperature using a Horiba Scientific spectrometer (Laboram HR Evolution model) with the excitation laser light of 514 nm.

3. Results and Discussion

The specific surface area of synthesized rGO sample of 465 m^2/g, determined through N_2 physisorption by applying the BET method to the data, was in agreement with the experimental measurements, reported within the range between 100 to 1000 m^2/g, for as-prepared graphene [18]. The obtained value of the specific surface area of rGO is sufficiently high, making it suitable for catalysts support purposes, indicating also the adequacy of the employed methodology of the rGO synthesis. The addition of Pd did not produce substantial changes in the specific surface area of Pd/rGO sample with the measured value of 428 m^2/g. Nevertheless, the Pd/CeO_2-rGO hybrid exhibited a striking drop in its specific surface area to about 160 m^2/g, which can be attributed to substantial changes in surface morphology of this sample. As presented later on in this study, mainly nanostructures of CeO_2 anchored in a nearly continuous manner on rGO form the surface morphology of the sample. Most probably, such a deposition of CeO_2 on rGO reduces the overall available surface of the sample for the physical adsorption of N_2.

The rGO formation was assessed by XRD analysis. The X-ray diffraction patterns obtained for GO (Fig. 1) after drying at 45 °C for 2h showed a peak around $2\theta = 12°$, denoting a periodicity of layer stacking (d-spacing of 0.729 nm) characteristic of graphene oxide structure.

After hydrothermal reduction (Fig. 2), the diffraction pattern of the recovered sample exhibited two broad peaks centered at 2θ values of 24.4°and 43.3°, marking the GO to rGO transformation typified by the removal of most of oxygen functionalities from initial GO structure. The peak at 24.4° (d-spacing of 0.364 nm) corresponds to graphite basal planes and exhibits a striking broadening, which can be originated from reduced size of coherently scattering domains and lattice microstrains, besides structural defects in graphene layers.

All these features indicate a strong structural disorder in rGO samples (aggregates of disoriented few-layered graphene nanosheets with eventual non-homogeneous deformations of crystal lattice). The X-ray diffraction patterns of Pd/rGO sample showed, in addition to graphene peaks, the peak at 2θ = 39.2° (d-spacing of 0.229 nm) corresponding to (111) diffraction line of metallic Pd^0. Furthermore, the addition of Pd resulted in an evident shift in 2θ position of the main peak of rGO phase, from about 24.4° (d-spacing of 0.365 nm) to 25.4° (d-spacing of 0.351 nm), which is indicative of a higher oxygen removal from GO in Pd/rGO sample. This effect is accompanied by a better structural ordering within the basal graphite planes as can be judged from better resolved and much more intense, as compared to rGO sample, peaks at 2θ of about 43°. These peaks correspond to Bragg reflections from (100), (101) and (102) crystallographic planes of hexagonal graphite structure. We estimated the mean dimension of the crystallites of Pd from the broadening of the (111) diffraction peak, under the assumption that all other contributions to peak broadening are negligible. One of the physically meaningful measures of the crystallite size is provided by the Stokes' and Wilson's equation [19]

$$L_V = \frac{\lambda}{B \cdot cos\theta}, \qquad (1)$$

where B is the integral breadth of the diffraction line (peak area divided by peak maximum), λ is the wavelength of the X-rays and θ is the half of the diffraction angle. This size is a sample average volume-weighted thickness of crystallites measured in the direction of X-ray scattering vector of a Bragg peak, and is often called apparent crystallite size [20]. The L_V value of 21.1 nm is obtained from (111) diffraction peak of Pd using equation 1. The estimate of real crystallite size from L_V depends on the shape and the size distribution of the crystallites. For monodisperse spherical crystallites with diameter D, the following relation is applicable: D = 4/3 L_V [21]. This later equation gives the diameter of 28.2 nm for Pd crystallites.

The above results indicate a formation of a synergistic environment during hydrothermal synthesis that leads to a simultaneous reduction of GO and palladium salt. The direct formation of Pd^0 in our catalyst system under hydrothermal synthesis is a motivating factor for the use of such a method for a synthesis of reduced metal nanoparticle as the active phase of catalysts employed in many relevant reactions of industrial processes. The hydrothermal route proves to be a promising approach to a one-step synthesis of rGO supported catalysts.

With regard to Pd/CeO_2-rGO sample, its XRD pattern shows well-defined peaks that can be perfectly described by the CeO_2 fluorite structure, together with the broad peak of rGO phase at 2θ of 25.4° (d-spacing of 0.351 nm). The most relevant feature of this diffraction pattern is the absence of diffraction peaks related to either Pd^o or PdO phases, suggesting that in this sample Pd is present in the form of a highly dispersed and very small-sized Pd species (clusters).

The difference in Pd phase morphology between Pd/rGO and Pd/CeO_2-rGO samples points out CeO_2 as a primary modifier of the dispersion of Pd during the synthesis. With the aim of understanding the exact morphology of the Pd dispersion and

possible interactions between the catalysts components, detailed TEM studies of Pd/rGO and Pd/CeO_2-rGO samples were performed. Representative HAADF-STEM images of the rGO sample (Fig. 3) showed the characteristic laminar structure of this material.

The selected images acquired for Pd/rGO are shown in Fig. 4 and Fig. 5. At low-magnification, HAADF-STEM images of the sample (Fig. 5a) exhibit small bright particles of varying sizes heterogeneously distributed over the rGO support. The Fourier filtered images of the isolated particles (insets in Fig. 4b and Fig. 4d) as well as the EDX spectra recorded from regions containing these particles (see Fig. 5c) conclusively identified them as metallic Pd with face-centered cubic crystal lattice. The micrographs disclosed a well-faceted morphology of Pd particles widely distributed in size (see Fig. 5b). The low-magnification bright-field TEM images (Figs. 4a and 4c) show characteristic sheets of rGO. The Pd particles are well in contact with the rGO support, as one can judge from the presence of rGO crystal planes around the Pd particles (Figs. 4b and 4d). The characteristic lattice spacing of 3.6 Å corresponding to the (002) crystallographic planes of rGO is readily obtained. The chemical interaction between Pd and rGO indicated by these results is in accordance with theoretical studies that predict the dependence of the strength of binding to rGO on the nature of the noble metal, being stronger for those with incomplete d orbitals [22]. However, a wide distribution of Pd particle size is readily observed in Pd/rGO sample.

The Pd/CeO_2-rGO sample appeared clearly different from Pd/rGO one, as disclosed by bright-field TEM images in by Fig. 6 and also by HAADF-STEM views (Fig. 7). Particles with two distinct morphologies can be seen over the rGO support (Fig. 6a and Fig. 6b): large aggregates of sizes from 10 nm to higher than 50 nm and very small particles of few nanometers homogeneously anchored onto the surface of

rGO. The lattice fringes of particles of both morphologies correspond only to crystallographic planes of CeO_2. Figures 6c and 6d show high-magnification images corresponding to regions “a” and “b” of Figure 6b. In the FT image of Figure 6c, the spots at 2.7 Å corresponds to the (200) crystallographic planes of CeO_2, while the intensity profile of the fringes of Figure 6d shows a d-spacing of 3.1 Å, which fits well to (111) crystallographic planes of CeO_2. The FT images of the larger aggregates also confirmed the CeO_2 crystalline identity of the observed particles (see Fig. 7c). We hypothesize that highly dispersed particles of ceria are those anchored to rGO surface, which can explain a nearly continuous and interconnected spatial distribution of CeO_2 species visible by TEM. Most probably, not only the extent of such a mosaic morphology of ceria particles correlates with the extent of the available rGO surface, but also the size of the coherent domains of fluorite-type CeO_2 structure correlates with the size of crystal domains of rGO sheets. Within this general picture of the relation between rGO and ceria morphologies, the larger particles of ceria detected in TEM images are those not bonded directly to rGO phase.

The picture of two essentially different (bimodal) size distributions of ceria particles revealed by TEM can explain the apparently inconsistent result of XRD analysis with respect to the size broadening of XRD peaks of the CeO_2 phase. Much broader diffraction peaks would be expected if only small crystallites of ceria (<5 nm) were present in the sample. Nevertheless, close inspection of the diffraction peak profiles of CeO_2 indeed shows very broad base of the peaks suggesting a superposition of size effects from distinct size distributions of crystallites. The smaller crystallites contribute to the observed XRD peaks with a broad signal centered at the Bragg-reflection position, while the larger ceria crystals produce much sharper distribution of the diffracted X-rays. The number of atoms in each system of ceria particles will define

the integrated intensity (respective peaks area) of each contribution to the overall peak intensity. It would be reasonable to admit that larger ceria particles contain more atoms than very small ones, even if the number of such particles is smaller. This is why the sharp component of peaks intensities prevails the overall profile of CeO_2 peaks observed in the XRD patterns. Palladium phase was almost invisible in the form of nanoparticles in Pd/CeO_2-rGO. Very sparsely distributed nanoparticles of about 2 nm size could be found (see Figure 8), whereas the rest of Pd was dispersed in entities below the resolution of HRTEM, which suggests the presence of dispersed Pd clusters and/or, eventually, single atoms as confirmed by EDS chemical analysis (see inset in Figure 8a).

The chemical analysis of Pd/CeO_2-rGO carried out by X-ray fluorescence confirmed the overall Pd load of about 5 wt%. Nearly the same relative intensity of Pd $K\alpha_{1,2}$ X-ray emission line was observed in both Pd-rGO and Pd/CeO_2-rGO XRF spectra (see inset in Figure 8b). This result and the absence of visible Pd particles by TEM in the Pd/CeO_2-rGO hybrid, strongly suggests that atomic clusters of Pd are formed and evenly distributed over the CeO_2-rGO support. The comparison of the TEM results from Pd/rGO and Pd/CeO_2-rGO samples unambiguously points out a remarkably promoting effect of ceria on Pd dispersion. The precise nature of such phenomena requires an additional investigation; however, the formation of highly dispersed CeO_2 on rGO (white spots in Figures 8a and 8b) is undoubtedly the key factor in the formation of sub-nanometer Pd clusters. High dispersion of CeO_2 on rGO by employing hydrothermal synthesis of CeO_2-rGO composites has been already reported in various experimental investigations [13, 14]. In these experiments, highly effective bonding observed between rGO and fine particles of CeO_2 was attributed to charge transfer interactions between rGO and CeO_2. The theoretical study by Xu et al. [23] found large amount of

charge transfer from rGO to CeO_2 well beyond the interface region. Such charge redistribution induces an increase of Ce^{3+} concentration and a concomitant increase of oxygen vacancy concentration in CeO_2. Oxygen vacancies that provide electroneutrality to nanoconfined volumes of CeO_2 do not result in any modification of the overall fluorite-type structure of CeO_2, as confirmed also by our XRD results. Nevertheless, a disorder in the oxygen sub-lattice, such as a nonstoichiometry, produce noticeable effects in the Raman spectrum of CeO_2. The bulk stoichiometric fluorite-structured CeO_2 has one Raman active mode in the first order spectrum, which correspond to a triply degenerated optical-phonon branch of F_{2g} symmetry at zone-center frequency around 465 cm^{-1} [23, 24]. The position of this line is shifted towards the lower wavenumbers (to 455 cm^{-1} in this study, see Fig. 9) in CeO_2 with disordered oxygen sub-lattice resulting from thermal effects, reduced particle size or doping [24, 26]. In addition, a substantial broadening of this peak is directly correlated with the reduction of a crystallite size of CeO_2 [24, 27]. The arguments that perturbations in fluorite-structure of CeO_2 are responsible for this effect are reinforced by the appearance of the weak bands (otherwise Raman inactive) corresponding to zone-center transverse doubly degenerated (IR active) and longitudinal optical modes [29, 30]. The respective frequencies of 272 cm^{-1} and 595 cm^{-1} defined in optical reflectivity studies [29, 31] of CeO_2 coincide well with the positions of the weak broad peaks observed in the Raman spectra of Pd/CeO_2-rGO sample of this work, and in the Raman spectra of CeO_2 of earlier studies [24, 26, 28]. All these Raman features may reflect a breakage of a local symmetry of Ce-O vibration units, caused by a high concentration of oxygen vacancies, which in turn modifies the Raman and infrared selection rules for vibrational modes of stoichiometric fluorite-structure of CeO_2.

The characteristic Raman features of graphene, as defects-induced D band and first-order Raman active G band observed at 1350 cm-^{1} and 1600 cm^{-1}, respectively, can provide important insights into the structural integrity of rGO support in Pd/CeO_2-rGO sample. The ratio of the intensities of these bands, I_D/I_G, combined with the G band spectral linewidth, Γ_G (measured as full width of the band at half the maximum), gives the possibility to distinguish structural disorder (low disorder/high disorder) of rGO [32,33]. The experimental studies confirm that these Raman characteristics allow for discerning the low disorder (stage 1) and high disorder (stage 2) states of oxidized graphene [19, 33, 34]. The evaluations of I_D/I_G ratios and Γ_G for GO, rGO, Pd/rGO and Pd/CeO_2-rGO samples show that oxidized graphene in all samples is highly disordered (stage 2). The disorder level is nearly similar for all the samples (Table 1), being somewhat higher for Pd/CeO_2-rGO sample. The obtained values of I_D/I_G ratios and Γ_G suggest that boundary defects (fragmentation of crystalline domains) dominate the overall defect structure of rGO [32]. Table 1, summaries the relevant Raman characteristics of D and G bands, together with the estimations of crystallite size from the Tuinstra and Koenig equation [35] that relates the I_D/I_G ratio to the crystallite size in polycrystalline graphitic samples, assuming the proportionality coefficient between the crystallite size and inverse I_D/I_G ratio from Knight and White [36].

Table 1 – Raman results for GO, rGO, Pd/rGO and Pd/CeO_2-rGO samples – I_D/I_G ratio and G band width values, Γ_G.

Sample	**Intensity**		**I_D/I_G**	**G band width, Γ_G (cm^{-1})**	**Crystallite Size, Tuinstra−Koenig (nm)**
	D	**G**			
GO	1.19	0.86	1.4	60	3.1
rGO	1.05	0.59	1.8	64	2.4

Pd/rGO	0.80	0.45	1.8	61	2.4
Pd/CeO_2-rGO	0.71	0.46	1.5	76	2.9

Small crystalline domains of reduced graphene preserve the in-plane crystal ordering in rGO and Pd/rGO samples, (see respective XRD patterns), while Pd/CeO_2-rGO samples does not show this feature despite the larger crystallite size estimated from Raman data. This difference can be caused by further disordering of the rGO support via formation of additional vacancies, dopants or functional chemical groups as the result of CeO_2-rGO interaction.

Finally, the thermal stability of the studied samples was investigated by TGA-MS analyses. Figure 10 depicts the results of TGA represented by the weight loss and the respective first derivatives. Only m/z ratios of 18 and 44, corresponding to H_2O and CO_2, respectively, were detected in all the samples. The mass spectra of CO_2 are shown in Figure 10c.The weight loss curves obtained for rGO and Pd/rGO were similar, while the thermal behavior presented by GO and Pd/CeO_2-rGO were entirely different from each other and all the other samples. The initial GO sample exhibited typical weight loss process composed of two main stages of the weight loss events. The first stage comprised the temperature interval between 150°C and 250°C, and the second one between 450°C and 550°C with the derivative peaks at 214 °C and 508 °C respectively. The thermal events of the first stage can be attributed to the decomposition of unstable groups of GO (hydroxyl, epoxy, carbonyl and carboxyl groups) [37]. At this step, H_2O (m/z=18) and CO_2 (m/z=44) are detected in the respective mass spectrum.

The second stage can be ascribed to the GO structure combustion, as revealed by CO_2 desorption peak centered at 518 °C in the mass spectrum. The thermal events in rGO sample above 150°C comprised only a broad derivative mass loss peak with maxima at 549 °C due to carbon lattice decomposition. For this sample, the total mass loss attained

almost 98%. The absence of thermal events between 150°C and 250°C related to decomposition of oxygenate groups indicates that they were efficiently removed from rGO sample by the hydrothermal treatment. The introduction of Pd into the sample resulted in the TGA spectrum which derivative exhibits the broad, split peak, slightly shifted towards lower temperatures with respect to the same peak of not modified rGO sample. Although Pd is known to be effective in catalyzing combustion reactions [38], its effect over rGO sample decomposition was small. This behavior can be associated with a metallic state of Pd in Pd/rGO compound confirmed by XRD and HRTEM studies, while PdO or PdO-Pd interface sites are normally involved in combustion reactions. The addition of CeO_2 to the catalyst led to a striking acceleration of the thermal degradation of the Pd/CeO_2-rGO sample as compared with Pd/rGO one. A weight loss of about 50% was observed between 300 °C and 400 °C with the derivative maximum at 320°C. Mainly CO_2 was detected at this event. We attribute this weight loss to the combustion of carbon skeleton.

In order to verify whether CeO_2 itself accelerates the combustion of rGO, TGA data on CeO_2-rGO sample were obtained as well. Close similarity of weight-loss curves of CeO_2-rGO and Pd/CeO_2-rGO samples (see Figure 10) undoubtedly indicate CeO_2 as a cause of this effect. Structural instability (breakage) of C-C bonds of aromatic carbon rings may arise due to a formation of reactive oxygen species such as hydroxyl radicals at the CeO_2-rGO interface. The excess of oxygen from CeO_2 may produce high-energy peroxide bridges C-O-O-C, which are a well-known source of such hydroxyl radicals [39]. Eventually formed nitrogen bridges and other nitrogen functionalities may also act as catalyst to reduce the energy barrier for C-C bonds rearrangement or breakage [40]. The overall weight loss of about 60% of CeO_2-rGO and Pd/CeO_2-rGO samples is consistent with the 30% load of CeO_2 in CeO_2-rGO and in Pd/ CeO_2-rGO. The thermal

stability exhibited by the Pd/CeO_2-rGO catalysts in this study make them promising for use as candidates for several catalytic reactions.

Although our data do not allow to infer the oxidation state of Pd in Pd/CeO_2-rGO sample, it is highly likely that PdO_x is stabilized in this hybrid, analogously to the numerous examples of synthesis of catalytic systems containing Pd/CeO_2 components (see [41, 42] to mention few). A detailed investigation of the structural and chemical properties of the components in $rGO/CeO_2/Pd$ system, especially the interfacial interactions, are under way.

4. Conclusions

In conclusion, the presence of rGO was essential for the formation of highly dispersed CeO_2 nanostructures on rGO surface, driving the Pd stabilization as small clusters in sub nanometer size range. Thus, specific interactions between rGO-CeO_2 and CeO_2-Pd is, most probably, responsible for such an uncommonly reported and highly desirable for catalytic application system. We believe that these results will motivate new studies on the optimization of this type of catalyst for the practical use and stimulate new investigations on synthesis of analogous catalysts systems based on other transition metals.

Acknowledgements

This work was supported by FAPESP (2018/18798-2). The authors also would like to thank to the undergraduate student Matheus Moura Nunes for his assistance during the GO and rGO synthesis experiments. JL is a Serra Húnter Fellow and is grateful to ICREA Academia program and projects MICINN/FEDER RTI2018-093996-B-C31 and GC 2017 SGR 128.

References

1. Wang, L,; Chen, W.; Zhang, D.; Du, Y.; Amal, R.; Qiao, S.; Wu, J.; Yin, Z. Surface strategies for catalytic CO_2 reduction: from two-dimensional materials to nanoclusters to single atoms, *Chem. Soc. Rev.* **2019,** 48, 5310-5349.

2. Bell, A. T. The impact of nanoscience on heterogeneous catalysis, *Science* **2003,** 299, 1688-1691.

3. Zaera, F. New challenges in heterogeneous catalysis for the 21st century, *Catal. Lett.* **2012,** 142, 501-516.

4. Liu, J. Catalysis by supported single metal atoms, *ACS Catal.* **2017**, 7 34−59.

5. Zhao, G.; Liu, H..; Ye, J. Constructing and controlling of highly dispersed metallic sites for catalysis, *Nano Today.* **2018,** 19 108–125.

6. Cheng, Y.; Fan, Y.; Pei, Y.; Qiao, M. Graphene-supported metal/metal oxide nanohybrids: synthesis and applications in heterogeneous catalysis, *Catal. Sci. Technol.* **2015,** 5, 3903-3916.

7. K. Kakaei, M. D. Esrafili, A. Ehsani, Graphene-Based Electrochemical, supercapacitors, *Interface Science and Tecnhology* **2019,** 27, 339-386.

8. Cheng, N.; Zhang, L.; Davis, K. D.; Sun. X. Single-Atom Catalysts: From design to application, *Electrochem. Energy Rev.* **2019,** 2, 539–573.

9. Farmer, J. A.; Campbell, C. T. Ceria maintains smaller metal catalyst particles by strong metal-support bonding, *Science*, **2010,** 329, 933-936.

10. Trovarelli, A.; Llorca, J. Ceria catalysts at nanoscale: how do crystal shapes shape catalysis, *ACS Catal.* **2017,** 7, 4716-4735.

11. Vayssilov, G. N.; Lykhach, Y. ; Migani, A.; Staudt, T.; Petrova, G. P.; Tsud, N.; Skála, T.; Bruix, A.; Illas, F.; Prince, K. C.; Matolın, V.; Neyman, K. M.; Libuda, J.

Support nanostructure boosts oxygen transfer to catalytically active platinum nanoparticles, *Nat. Mater*. **2011,** 10, 310-315.

12. Zhou, X.-D.; Huebner, W. Size-induced lattice relaxation in CeO_2 nanoparticles, *Appl. Phys. Lett.* **2001,** 79, 3512-3514.

13. Ji, Z.; Shen, X.; Li, M.; Zhou, H.; Zhu, G.; Chen, K. Synthesis of reduced graphene oxide/CeO_2 nanocomposites and their photocatalytic properties, *Nanotechnology* **2013,** 24, 115603 (9pp).

14. Jiang, L., Yao, M.; Liu, B.; Li, Q.; Liu, R.; Lv, H.; Lu, S.; Gong, C.; Zou, B.; Cui, T.; Liu, B. Controlled synthesis of CeO_2/graphene nanocomposites with highly enhanced optical and catalytic properties, *J. Phys. Chem. C* **2012,** 116, 11741 – 11745.

15. Srivastava, M.; Das, A. K.; Khanra, P.; Uddin, M. E.; Kim, N. H.; Lee, J. H. Characterizations of in situ grown ceria nanoparticles on reduced graphene oxide as a catalyst for the electrooxidation of hydrazine, *J. Mater. Chem. A* **2013,** 1, 9792–9801.

16. Sun, T.; Xiao, J.; Chen, C.; Xiao, F.; Wang, S.; Liu, Y. Facile and green synthesis of palladium nanoparticles-graphene-carbon nanotube material with high catalytic activity, *Sci. Rep.* **2013,** 3:2527, 1-6.

17. Xu, Y.; Sheng, K.; Li, C.; Shi, G. Self-assembled graphene hydrogel via a one-Step, *ACS Nano* **2010,** 4(7), 4324-4330.

18. Stankovich, S.; Dikin, D. A.; Piner, R. D.; Kohlhaas, K. A.; Kleinhammes, A; Jia, Y.; Wu, Y.; Nguyen, S. T.; Ruof, R. S. Synthesis of graphene-based nanosheets via chemical reduction of exfoliated graphite oxide *Carbon* **2007**, 45 1558-1565.

19. Stokes, A. R.; Wilson, A. J. C. A method of calculating the integral breadths of Debyee Scherrer lines, *Math. Proc. Cambridge Philos. Soc.* **1942,** 38, 313-322.

20. Langford, J. I.; Wilson, A. J. C. Scherrer after sixty years: a survey and some new results in the determination of crystallite size, *J. Appl. Crystallogr.* **1978,** 11, 102-113.

21. Balzar, D. Profile fitting of X-ray diffraction lines and fourier analysis of broadening, *J. Appl. Crystallogr*. **1992,** 25, 559–570.

22. Navalon, S., Dhakshinamoorthy, A., Alvaro M., Garcia, H. Metal nanoparticles supported on two-dimensional graphenes as heterogeneous catalysts, *Coord. Chem. Rev.* **2016,** 312, 99–148.

23. Xu, L.; Huang, W.Q.; Wang, L. L.; Huang, G.F. Interfacial interactions of semiconductor with graphene and reduced graphene oxide: CeO_2 as a case study, *ACS Appl. Mater. Interfaces* **2014,** 6, 20350−20357.

24. Weber, W. H.; Bass, K. C.; McBride, J. R. Raman study of CeO_2: Second-order scattering, lattice dynamics, and particle-size effects, *Phys. Rev.* **1993,** 48(1), 178-185.

25. Buckeridge, J.; Scanlon, D. O.; Walsh, A.; Catlow, C. R. A.; Sokol, A. A. Dynamical response and instability in ceria under lattice expansion, *Phys. Rev. B* **2013,** 87, 214304.

26. Brogan, M. S.; Dines, T. J.; Cairns, J. A. Raman spectroscopic study of the Pt–CeO_2 interaction in the Pt/Al_2O_3–CeO_2 catalyst, *Chem. Soc. Faraday Trans* **1994,** 90, 1461-1466.

27. Graham, G. W.; Weber, W. H.; Peters, C. R.; R. Usmen, Empirical method for determining CeO_2-particle size in catalysts by Raman spectroscopy, *J. of Catal.* **1991,** 130, 310-313.

28. Swatsitang, E.; Phokha, S.; Hunpratub, S.; Maensiri, S. Modification of Ce valence states by Sm/Sr co-doping of CeO_2 nanoparticles for improved magneto-electrochemical properties, *Mater. Des.* **2016,** 108, 27–33.

29. Mochizuk, S. Infrared optical properties of cerium dioxide, *Phys. Stat. Sol. (b)* **1982,** 114, 189-199.

30. Ganesan, S.; Burstein, E. Selection rules for second order infrared and raman processes. II. Fluorite structure and the interpretation of the second order infrared and Raman spectra of CaF_2, *J. Phys.* **1965,** 26 (11), 645-648.

31. Marabelli, F. Covalent insulator CeO_2: Optical reflectivity measurements *Phys. Rev. B* **1987,** 36 (2), 1238-1243.

32. Cançado, L. G.; da Silva, M. G.; Ferreira, E. H. M.; Hof, F.; Kampioti, K.; Huang, K.; Pénicaud, A.; Achete, C. A.; Capaz, R. B., Jorio, A. Disentangling contributions of point and line defects in the Raman spectra of graphene-related materials, *2D Mater.* **2017,** 4, 025039.

33. Eigler, S.; Dotzer, C.; Hirsch, A. *Carbon* **2012,** 50, 3666–3673.

34. Mendoza, M. E.; Ferreira, E. H. M.; Kuznetsov, A.; Achete, C. A.; Aumanen, J.; Myllyperkio, P.; Johansson, A.; Pettersson; M.; Archanjo, B. S. *Carbon* **2019,** 143, 720-727.

35. Tuinstra, F.; Koenig, J. L. Raman spectrum of graphite, *J. Chem. Phys.* **1970,** 53 1126-1130.

36. Knight, D. S.; White, W. B. Characterization of diamond films by Raman spectroscopy, J. Mater. Res. **1989,** 4, 385-393.

37. Moussa, S.; Siamaki, A. R.; Gupton, B. F.; El-Shall, M. S. Pd-partially reduced graphene oxide catalysts (Pd/PRGO): Laser synthesis of Pd nanoparticles supported on PRGO nanosheets for carbon–carbon cross coupling reactions, *ACS Catal.* **2012,** 145-154.

38. McCarty, J. G. Kinetics of PdO combustion catalysis, *Catal. Today* **1995,** 26 283.

39. Jeong, H. K., Lee, Y. P.; Lahaye, R. J. W. E.; Park, M. H.; An, K. H.; Kim, I. J.; Yang, C. W.; Park, C.Y.; Ruoff, R. S.; Lee, Y. H. Evidence of graphitic AB stacking order of graphite oxides, *J. Am. Chem. Soc.* **2008,** 130, 1362-1366.

40. Li, X. F.; Lian, K. Y.; Liu, L.; Wu, Y.; Qiu, Q.; Jiang, J.; Deng.; M Luo, Y. Unraveling the formation mechanism of graphitic nitrogen-doping in thermally treated graphene with ammonia, *Sci. Rep.* **2016,** 6, 23495-23505.

41. Colussi, A; Trovarelli, A.; Vesseli, E.; Baraldi, A.; Comelli, C.; Groppi, G.; Llorca, J. Structure and morphology of Pd/Al_2O_3 and $Pd/CeO_2/Al_2O_3$ combustion catalysts in Pd–PdO transformation hysteresis, *Appl. Catal. A* **2010,** 390, 1–10.

42. Schwartz, W. R.; Pfefferle, L. D. Combustion of Methane over Palladium-Based Catalysts: Support Interactions. *J. Phys. Chem. C* **2012,** 116, 8571-8578.

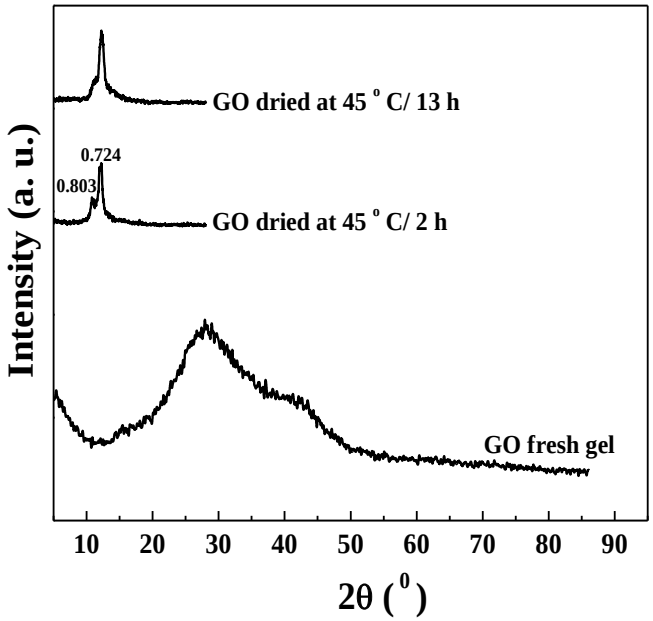

Figure 1 - XRD patterns of graphene oxide (GO) as gel; dried at 45 °C for 2 and 13 h under He flow.

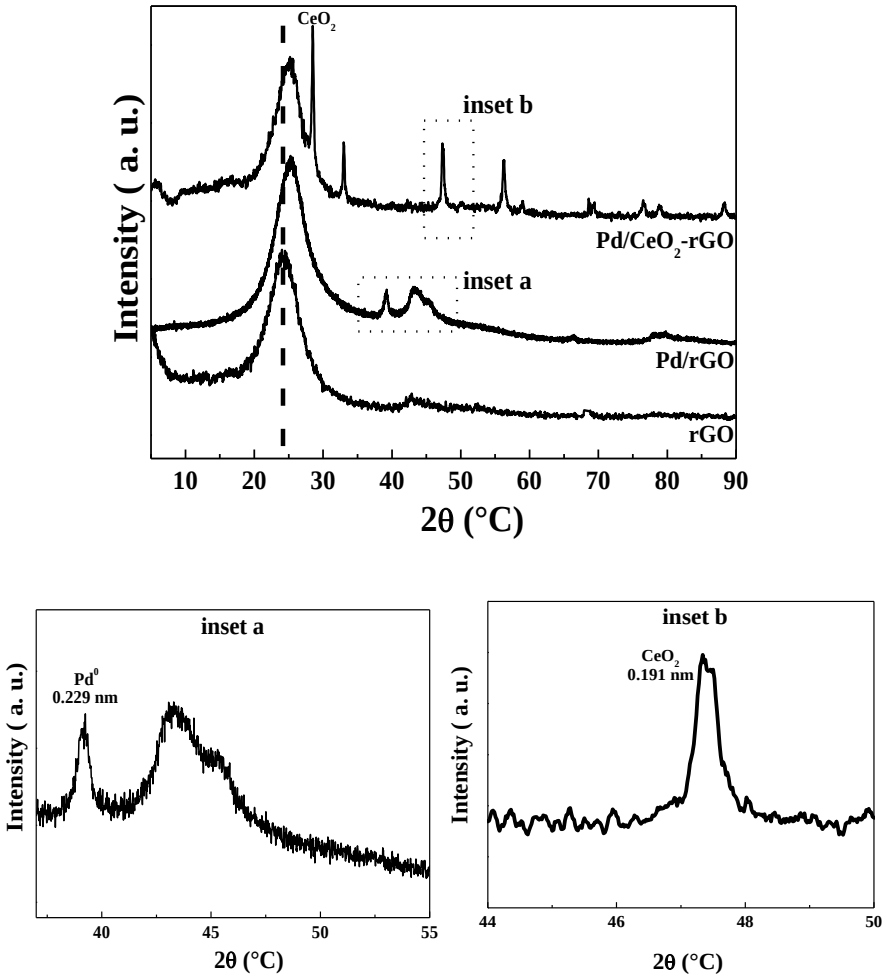

Figure 2 - XRD diffraction patterns of rGO, Pd/rGO and Pd/CeO_2-rGO.

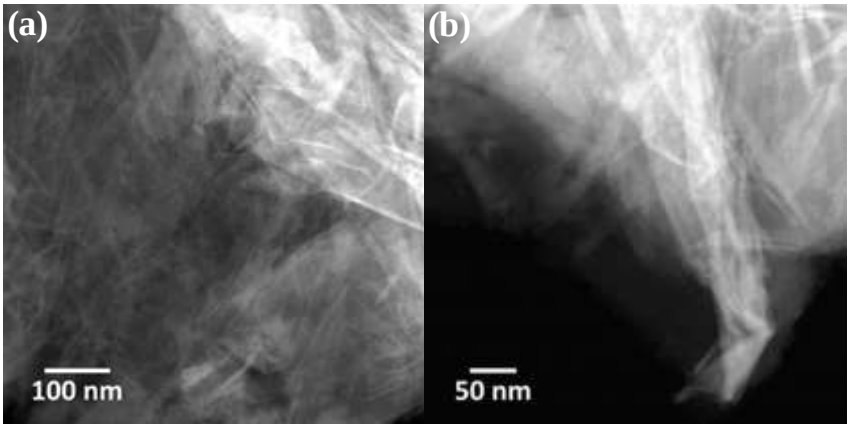

Figure 3 – Representative HAADF-STEM images of the rGO sample.

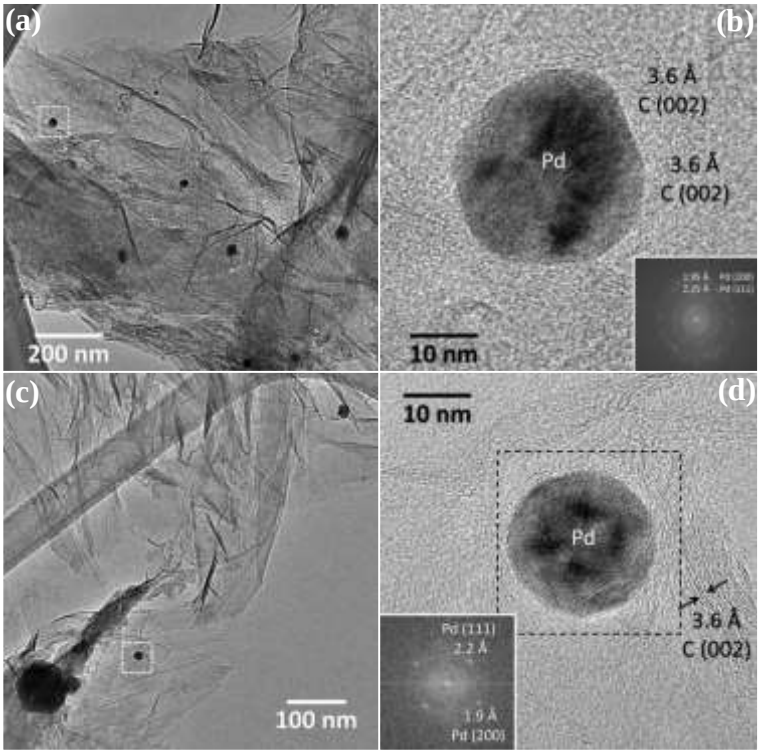

Figure 4 – Transmission Electron Microscopy of Pd/rGO catalyst: **(a)** and **(c)** Low-magnification bright-field TEM images **(b)** and **(d)** HRTEM and FT images of the particles inside the white rectangles in (a) and (c), respectively.

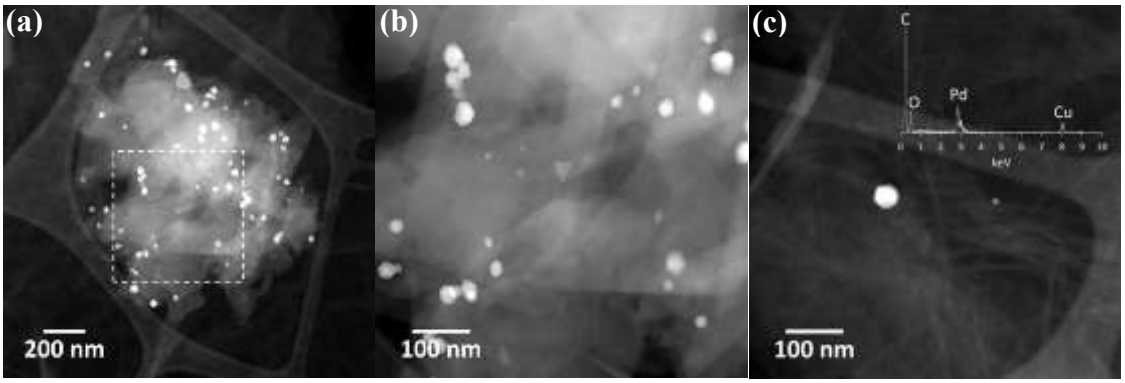

Figure 5 – HAADF-STEM images of the sample Pd/rGO at **(a)** Low-magnification **(b)** higher magnification and **(c)** EDX spectrum recorded on the bright particle shown in the image.

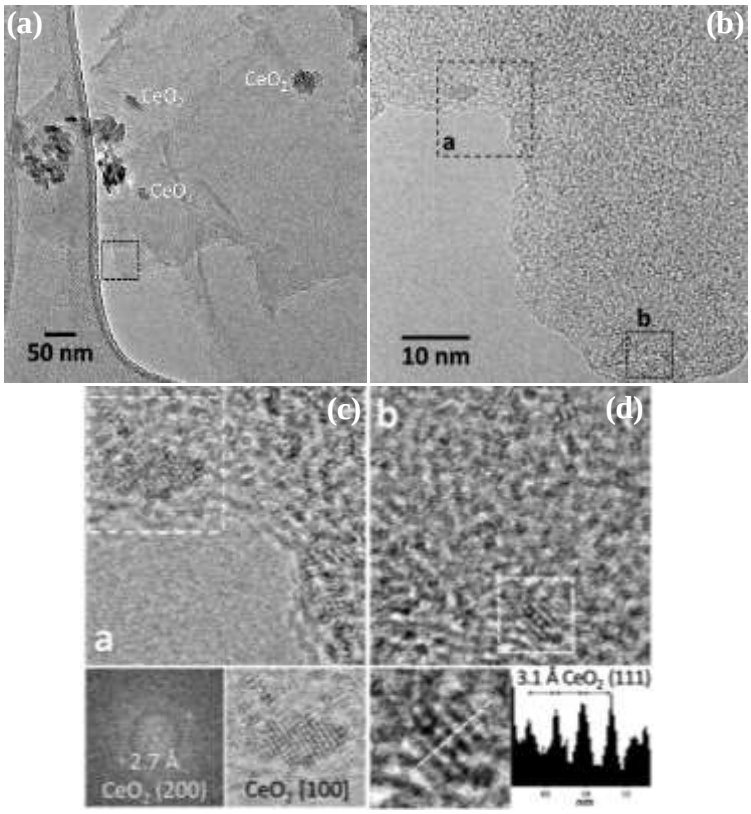

Figure 6 – Transmission Electron Microscopy of Pd/CeO_2-rGO catalyst **(a)** Low-magnification bright-field TEM images **(b)** High-magnification bright-field TEM images **(c)** FT images and the profile analysis of the area labeled as "a" in **(b)**. **(d)** FT images and the profile analysis of the area labeled as "b" in **(b)**.

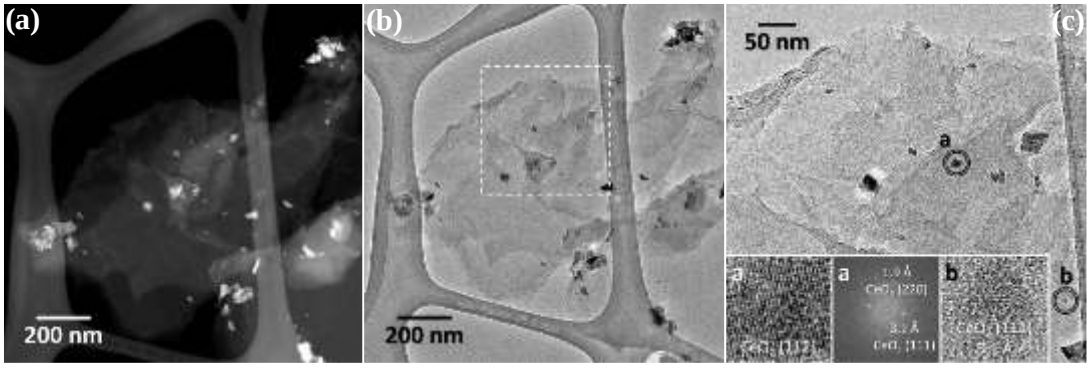

Figure 7 – Sample Pd/CeO_2-rGO **(a)** HAADF-STEM view of the sample **(b)** The same area of the sample in bright-field mode; **(c)** HRTEM images of particles "a " and "b" are shown in HRTEM mode in the insets, along with the FT image of particle "a" and ¨b¨.

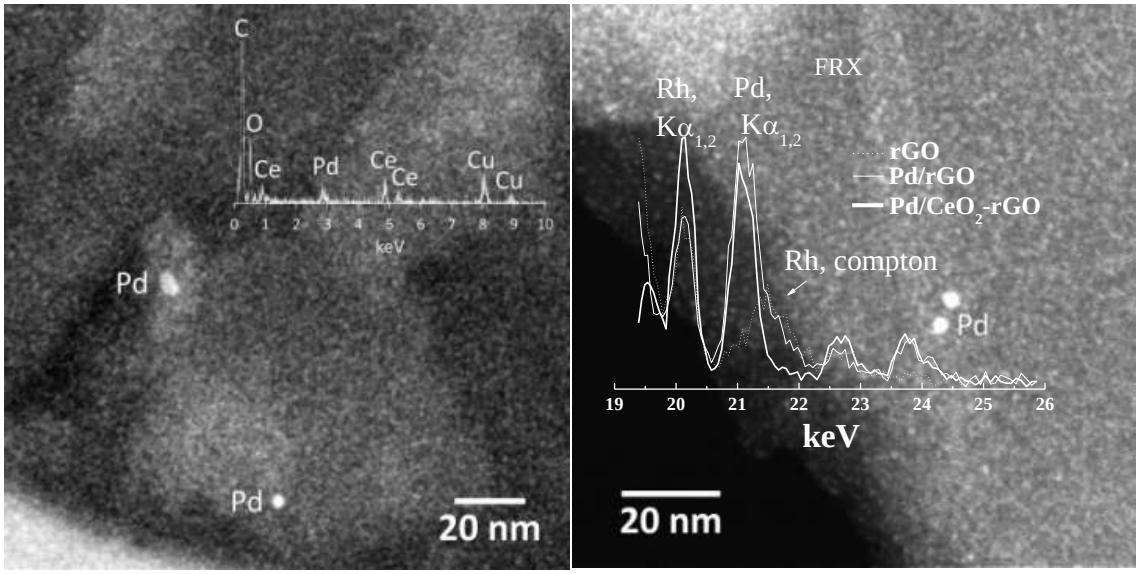

Figure 8 – (a) and **(b)** HAADF-STEM images recorded for Pd/CeO_2-rGO.

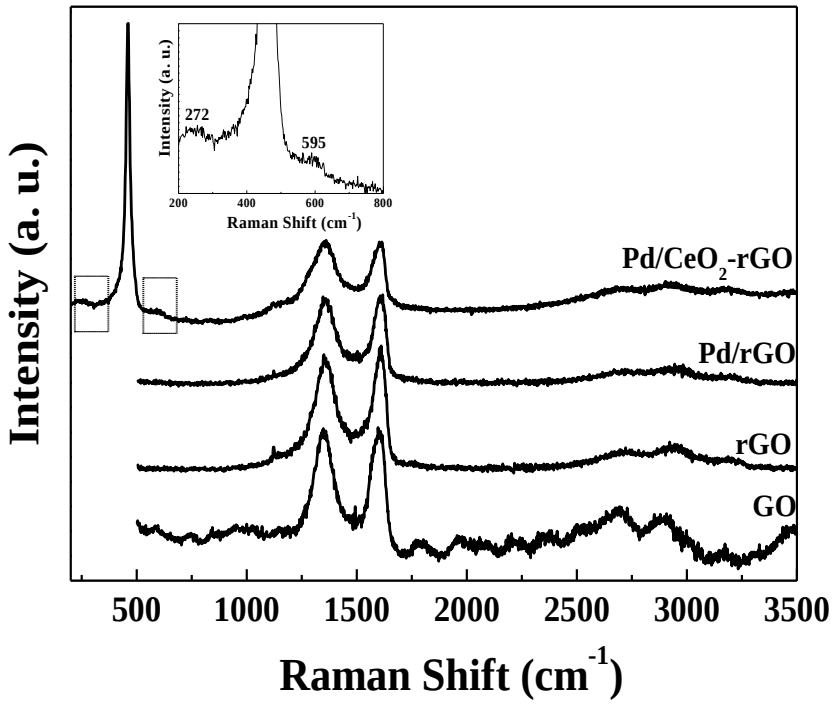

Figure 9 – Raman Spectra of GO, rGO, Pd/rGO and Pd/CeO_2-rGO.

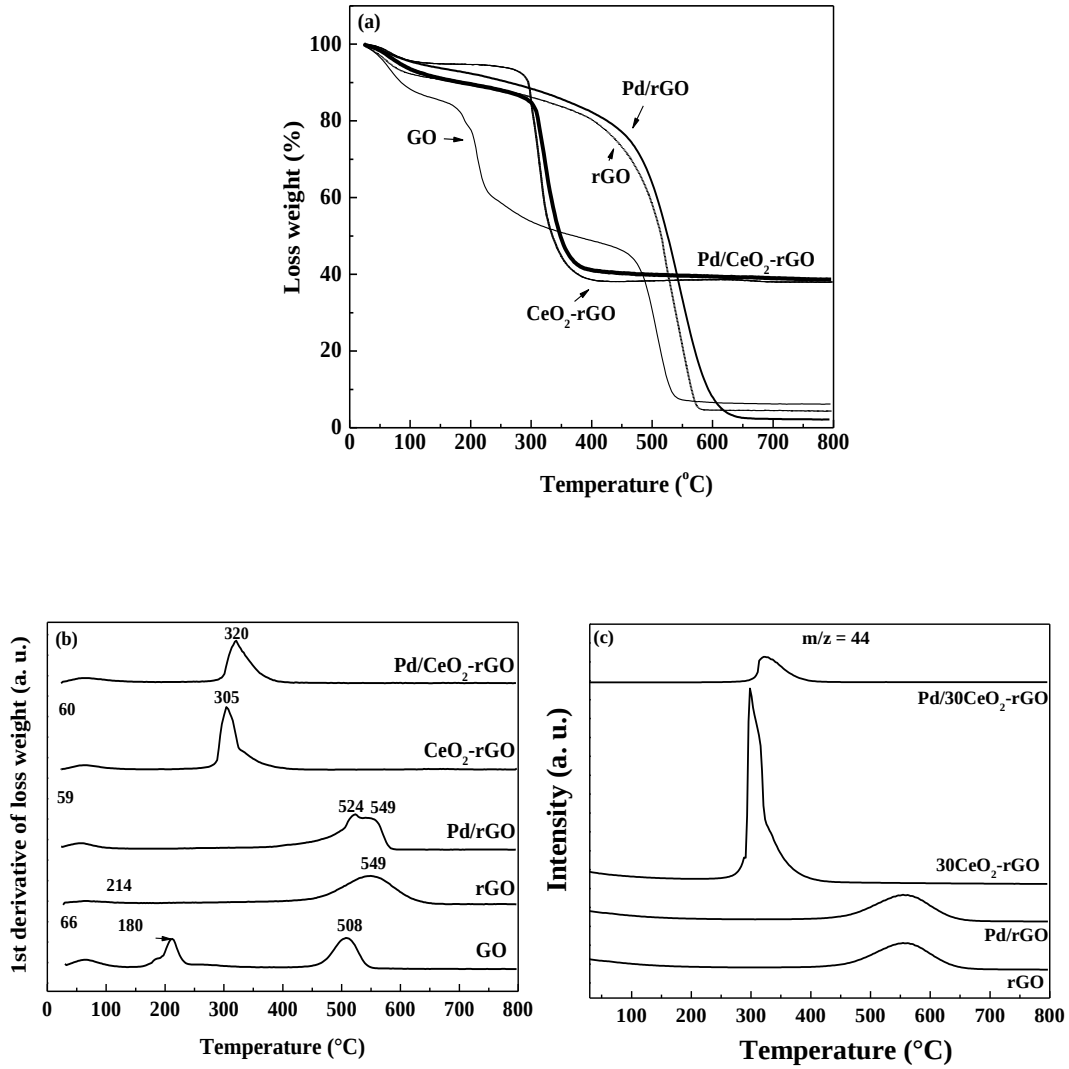

Figure 10 – Thermogravimetric analysis of the rGO and rGO supported catalysts **(a)** Loss weight profiles **(b)** First derivative of the loss weight profiles and **(c)** CO_2 spectra (m / z = 44) evolution for all the samples.